

Performance enhancement of rechargeable zinc-air battery through synergistic ex-solution of multi-component Pt/CoWO_{4-x} catalysts

Changho Lee^{a,b}, Chang-Kyu Hwang^c, Jung-Won An^d, Ji-Soo Jang^d, Bonjae Koo^e,
Jong Min Kim^c, Kihyun Shin^f, Caroline Sunyong Lee^{b,*}, Ki Ro Yoon^{a,b,**}

^a Textile Innovation R&D Department, Korea Institute of Industrial Technology, 143, Hangeul-ro, Sangnok-gu, Ansan-si, Gyeonggi-do 15588, Republic of Korea

^b HYU-KITECH Joint Department, Hanyang University, 143, Hangeul-ro, Sangnok-gu, Ansan-si, Gyeonggi-do 15588, Republic of Korea

^c Materials Architecturing Research Center, Korea Institute of Science and Technology (KIST), 14-gil 5 Hwarang-ro, Seongbuk-gu, Seoul 02792, Republic of Korea

^d Electronic Materials Research Center, Korea Institute of Science and Technology (KIST), Seongbuk-gu, Seoul 02792, Republic of Korea

^e School of Chemistry and Energy, Sungshin Women's University, Seoul 01133, Republic of Korea

^f Materials Science and Engineering, Hanbat National University, 125 Dongseo-daero, Yuseong-gu, Daejeon 34158, Republic of Korea

ARTICLE INFO

Keywords:

Bifunctional electrocatalyst
Electrospinning
Multi-component ex-solution
Catalyst-support hybrid
Zinc-air battery

ABSTRACT

Advancing zinc-air battery (ZAB) technology necessitates the development of air cathode electrocatalyst systems that demonstrate high reactivity and stability. We introduce a novel method to fabricate a robust catalyst-support hybrid. This hybrid comprises Co-doped Pt nanoparticles (NPs) anchored on metal oxide (Ex-PtCoWO) nanofibers (NFs), synthesized via electrospinning followed by selective metal ex-solution. Controlling the ex-solution of metal NPs leads to a highly active and stable oxygen reduction reaction (ORR). Moreover, the three-dimensional CoWO_{4-x} NFs network enhances the surface exposure of ex-solved metal NPs, thereby aiding both selective ex-solution and the provision of active sites for the oxygen evolution reaction (OER) during ZAB recharge. The Ex-PtCoWO NF exhibits an ORR half-wave potential of 0.89 V and an OER potential of 1.69 V at 10 mA cm⁻² in alkaline media. ZABs utilizing Ex-PtCoWO NF show an extended cycle life of over 240 h with reduced charge-discharge polarization, compared to commercial catalysts.

1. Introduction

Rechargeable zinc-air batteries (ZABs) are emerging as next-generation energy storage devices due to their superior theoretical energy density (~1218 Wh kg⁻¹), which surpasses that of practical lithium-ion batteries (~400 Wh kg⁻¹). This advantage, combined with their inherent safety from the use of aqueous electrolytes and cost competitiveness (10 \$ kW⁻¹ h⁻¹) derived from the abundance of zinc metal anodes, positions ZABs favorably [1–3]. However, their practical application faces challenges, primarily the poor cycle life caused by sluggish cathode reactions, specifically the oxygen reduction reaction (ORR) and oxygen evolution reaction (OER) during discharging and charging, respectively [4,5]. Traditional air cathode catalysts, employing novel metals such as Pt and metal oxides such as IrO₂ and RuO₂ with carbonaceous supports, have shown degradation in catalytic activity due to agglomeration or detachment from the supports and carbon support

oxidation or corrosion, prompting the exploration of highly active and sustainable catalyst-support systems [6–8].

To address the limitations of carbonaceous supports, inorganic metal-based supports such as oxides, carbides, nitrides, borides, and layered double hydroxides have been actively investigated [9–12]. These materials offer significant advantages, including robustness, corrosion resistance, and an effective platform for enhancing catalyst activity. While metal oxides such as TiO_{2-x} have received considerable attention, research focusing on combinations of metal oxides and nanoparticles (NPs) is gaining momentum [13]. However, the low electrical conductivity of metal oxides poses a challenge for their use as supports, necessitating facile electron transport. Combinations of metal catalysts with carbides (e.g., Pt/Mo₂C, Pt/WC) or nitride supports (e.g., Ir/Co₄N, Ru/NiWN_x, Pt/TiN) have been proposed, but challenges in thermal treatment and ensuring long-term stability under specific operating conditions remain critical for broad commercialization

* Corresponding author.

** Corresponding author at: Textile Innovation R&D Department, Korea Institute of Industrial Technology, 143, Hangeul-ro, Sangnok-gu, Ansan-si, Gyeonggi-do 15588, the Republic of Korea.

E-mail addresses: sunyonglee@hanyang.ac.kr (C.S. Lee), kryoon@kitech.re.kr (K.R. Yoon).

<https://doi.org/10.1016/j.apcatb.2024.124371>

Received 19 March 2024; Received in revised form 19 June 2024; Accepted 4 July 2024

Available online 5 July 2024

0926-3373/© 2024 The Authors. Published by Elsevier B.V. This is an open access article under the CC BY-NC license (<http://creativecommons.org/licenses/by-nc/4.0/>).

[14–18].

Kim and Yoon et al. recently developed a straightforward fabrication process for highly conductive black tungsten oxide (WO_{3-x}) nanofiber (NF) supports for fuel cell catalysts. This process involves thermal reduction during calcination to increase oxygen vacancies, thereby reducing the intrinsic band gap and enhancing the electrical conductivity of the supports. The increased oxygen vacancies on the surface of WO_{3-x} NFs also allowed for the accommodation of an extremely high mass loading of Pt NPs (~5 nm in size), demonstrating high ORR activity and durability in HClO_4 solution and highlighting potential of WO_{3-x} in electrocatalysis applications [19]. The versatility and distinctive surface activity of WO_{3-x} have led to its widespread use in various fields, including gas sensors [20], photocatalysts [21], and electrocatalysis in ZABs [22–24]. However, challenges such as NP detachment or agglomeration during synthesis persist, often due to low interfacial stability between different catalyst and support phases, as well as the redox reaction mechanism involving repeated dissolution, particularly during ZAB discharge and charge reactions [25].

The ‘ex-solution’ phenomenon has been identified as a promising synthesis method for achieving uniformly dispersed metal NPs on metal oxide supports, effectively preventing agglomeration through their socket-like coupling [26,27]. This process involves the selective precipitation of metal ions from the host oxide to the surface through a single heat treatment [28]. Metal NPs formed by ex-solution exhibit exceptional thermal and chemical stability, along with uniform particle size distribution, proving useful in applications like solid oxide fuel cells, electrolyzers and gas sensors [29–31]. Despite the focus on well-structured dopants and supports, an increasing interest in exploring a wider range of materials has emerged, including nanostructured and various-component systems, for the investigation of similar ex-solution behavior and expand potential applications. Jang et al. have recently demonstrated the potential of WO_3 as a host oxide for ex-solution in gas sensors [32]. Notably, the reduction of WO_3 is accelerated in the presence of an Ir component, and the ex-solution of Ir NPs is dynamically occurring. Thus, exploring various combinations with WO_3 is deemed crucial.

Herein, we propose a simple fabrication process for a cobalt and tungsten-based oxide NF with ex-solved Co-doped Pt NPs on the surface, creating a highly durable bifunctional catalyst-support hybrid material for ZABs air cathode. This hybrid material is produced through the electrospinning of a single polymer solution followed by step-wise thermal treatments. The thermally reduced Pt/CoWO_{4-x} (Ex-PtCoWO) NF hybrid exhibits excellent bifunctional performance in half-cell tests, attributed to the selective ex-solution of Co-doped Pt NPs. The Co-doped Pt NPs facilitate reactant accommodation for ORR and electron transport through a strongly adhered CoWO_{4-x} support, ensuring high reactivity over an extended period. Furthermore, the three-dimensionally networked CoWO_{4-x} ($0 < x \leq 1$) NF increases the surface exposure of ex-solved metal NPs, acting as a medium for selective ex-solution and providing active sites for OER. This Co-doped Pt-anchored CoWO_{4-x} NF hybrid functions synergistically as a single catalyst unit for both ORR and OER, delivering high coulombic efficiency in repeated discharge-charge cycles (over 240 hours) in ZABs and outperforming cells using commercial ‘Pt/C + IrO₂’ mixed catalysts. These results offer a methodology for the facile production of nanostructured, ex-solved multi-component catalyst-support hybrids and provide a design strategy for air cathodes, contributing to the practical implementation of ZABs.

2. Experimental section

2.1. Materials

Tungsten (VI) chloride (WCl_6 , 99.9%), polyvinylpyrrolidone (PVP, Mw = 1300,000), acetic acid (CH_3COOH , reagent plus, >99%), platinum chloride (PtCl_4 , >99%), cobalt acetate hydroxide ($\text{Co}(\text{CH}_3\text{CO}_2)_2 \cdot 4 \text{H}_2\text{O}$), 20% Pt/C, and IrO₂ were purchased from Sigma-

Aldrich. N, N-dimethylformamide (DMF, anhydrous, 99.8%) was purchased from DAEJUNG chemical & metals. All materials were used as received without further purification.

2.2. Synthesis of PtWO, CoWO and PtCoWO NFs

The fabrication of PtWO, CoWO, and PtCoWO NFs involved electrospinning and subsequent thermal treatments. Initially, a mixture of 1.5 g of WCl_6 and 1.5 g of PVP was dissolved in 10 g of DMF, stirred for 24 h until complete dissolution. The solution, transparent with a cobalt blue color, was subsequently augmented with 216 mg of PtCl_4 , 306 mg of $\text{Co}(\text{CH}_3\text{CO}_2)_2 \cdot 4\text{H}_2\text{O}$, and 0.25 g of CH_3COOH . For PtWO NF, only the Pt precursor (216 mg) was added, whereas CoWO NF incorporated solely the Co precursor (306 mg) into the WCl_6 polymer solution. This mixture was magnetically stirred overnight to ensure homogeneity. The solution was transferred to a 10 mL syringe equipped with a 25 G stainless steel needle for electrospinning. The solution was injected at a rate of 0.2 mL h⁻¹, with a working distance of 15 cm from the needle tip to a grounded substrate. An electric field, generated by a 15 kV high DC voltage, facilitated the ejection of the solution from the needle tip, enabling the collection of electrospun NFs on an aluminum foil substrate. The as-spun NFs were dried in an oven at 60 °C for 1 h to adequately evaporate residual solvents. The resulting composite NFs were calcined at 400 °C for 1 h at a heating rate of 5 °C min⁻¹ in ambient air. This step was crucial to remove polymeric components and crystallize oxide materials, culminating in the formation of Pt and Co-dissolved WO_3 -based NFs.

2.3. Synthesis of Ex-PtWO, Ex-CoWO and Ex-PtCoWO NFs

To induce the ex-solution process in PtCoWO NFs, a reduction heat treatment was conducted in a 4% H₂/Ar atmosphere. This process spanned 1 h within a temperature range of 500–800 °C, employing 100 °C intervals and a heating rate of 5 °C min⁻¹. The resulting NFs were labeled as Ex-PtCoWO 000 NFs, with 000 representing the specific reduction temperature. Parallely, Ex-PtWO 700 NF and Ex-CoWO 700 NF were synthesized under identical conditions. This approach was adopted to facilitate a comparative analysis of their electrochemical performance with Ex-PtCoWO 700 NF. The synthesis details comparisons are thoroughly outlined in Table S1.

2.4. Characterizations

The morphological characteristics of the fabricated hybrid materials were examined using various advanced microscopic techniques. Field emission scanning electron microscopy (FE-SEM; SU8010, Hitachi Co., Japan), transmission electron microscopy (TEM; JEM-ARM200F, JEOL, Japan), and Titan Double Cs corrected TEM (Titan cubed G2 60–300, FEI Co., USA) were employed for detailed morphological observation. Thermogravimetric analysis (TGA; Q500, TA Instruments, USA) was performed to assess the thermal stability and decomposition patterns of the materials. This analysis was conducted with a heating rate of 20 °C min⁻¹ in a mixed N₂/O₂ atmosphere (7:3 v/v) over a temperature range of 25–900 °C. A UV–Vis spectrophotometer (V770; JASCO, Japan) was used to measure the optical absorbance and determine the bandgap energy. Chemical bonding states within the materials were investigated via X-ray photoelectron spectroscopy (XPS; K-Alpha, Thermo Scientific™, USA) equipped with Al K α radiation (1486.6 eV). The crystalline structures of the materials were characterized using high-resolution powder X-ray diffraction (XRD; D/Max–2500/PC, Rigaku with a Cu K α radiation source; $\lambda = 1.5418 \text{ \AA}$, Japan). Additionally, phase transitions occurring during calcination were monitored by high-temperature in-situ XRD (X’Pert PRO, Malvern Panalytical with a Cu K α radiation source; $\lambda = 1.5418 \text{ \AA}$, USA). For surface structure analysis, O₂ temperature programmed desorption (O₂-TPD) was conducted using a Microtrac MRB instrument (BELCAT, USA). The Brunauer–Emmett–Teller

(BET) surface area of the NFs was evaluated using a surface area analyzer (BET; ASAP 2010, Micromeritics, USA). Electron paramagnetic resonance (EPR) experiments were conducted with by using an X-band spectrometer (Bruker EMX/plus spectrometer, Germany) at low temperature (-100 °C) and a frequency of operating 9.65 GHz. Furthermore, to probe the local atomic structure and bond lengths related to the adsorbing atoms, Extended X-ray Absorption Fine Structure (EXAFS) measurements were carried out at the hard X-ray 1D X-ray absorption spectroscopy (XAS) KIST-PAL beamline, located at the Pohang Accelerator Laboratory. The facility operates at 3.0 GeV with a maximum storage current of 360 mA. The collected EXAFS data were processed using the ATHENA software and simulated with ARTEMIS.

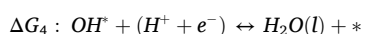
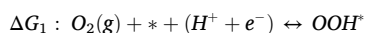
2.5. Computational details

Spin-polarized density functional theory (DFT) calculations were conducted using the Vienna ab initio simulation package (VASP) [33–35], based on a plane wave basis set. The calculations set a cut-off energy of 400 eV. To determine the electron exchange and correlation energy, the generalized gradient approximation (GGA)-level revised Perdew–Burke–Ernzerhof functional (RPBE) was employed [36–38]. The Brillouin zone sampling adhered to a $2 \times 2 \times 1$ k-point mesh, following the Monkhorst-Pack scheme. The convergence criteria for electronic and geometrical optimization were established at 10^{-5} eV and 10^{-2} eV Å⁻¹, respectively. To elucidate the ex-solution mechanism, two distinct systems based on the monoclinic CoWO₄ (100) slab model were constructed. The first system, referred to as the PtCoWO₄ (100) system (denoted as PtCoWO₄), was designed to determine which element surfaces first during the ex-solution process. The second system featured a Pt NP supported on the CoWO₄ (100) system (labeled as Pt/CoWO₄), post-Pt ex-solution (refer to Fig. S1). This model aimed to assess the influence of Pt NP on Co ex-solution. Each slab system comprised three repeating layers, with one bottom layer fixed in its bulk position. These systems were centered in a 20 Å vacuum gap along the z-direction. The oxygen vacancy formation energy (E_{vac}) was calculated using Eq. (1).

$$E_{vac} = E_{slab \text{ with vacancy}} + E_{oxygen} - E_{slab} \quad (1)$$

where $E_{slab \text{ with vacancy}}$ was the total energy after oxygen vacancy formation, E_{oxygen} was the gas phase energy of oxygen, and E_{slab} was the total energy of the stoichiometric surface.

To evaluate the catalytic activity of ORR and OER, we investigated three different systems based on the ex-solution process described above: CoWO₄, PtCoWO₄, and PtCo alloy NPs supported on the CoWO₄ slab (referred to as PtCo/CoWO₄). Simple clusters composed of 5 atoms were modeled to distinguish the effect of alloying (refer to Fig. S1). Reaction energy diagram for ORR and OER were plotted to determine the overpotential, serving as a simple descriptor for comparing activity in DFT calculations. The changes in Gibbs free energy (ΔG) for each reaction step in ORR (with the reverse reaction is OER) were calculated as follows:



The ORR and OER overpotential (η_{ORR} , η_{OER}) were determined from the reaction energy diagram using the following equation [39–41].

$$\Delta G(U) = \Delta E + \Delta ZPE - T\Delta S + neU$$

Where ΔE is the reaction energy, ΔZPE is the zero-point energy correction, ΔS is the change in entropy, and U is the applied potential. The chemical potential of the solvated proton and electron pair ($H^+ + e^-$)

under standard conditions ($p_{H_2} = 1$ bar, $a_{H^+} = 1$, $T = 298.15$ K) was calculated as $0.5\mu_{H_2(g)}^0 - eU$, assuming equilibrium at the standard hydrogen electrode [41,42].

2.6. Electrochemical measurements

Electrochemical performance assessments were conducted using a three-electrode system, which included an electrode rotator (RRDE-3A, ALS) and a potentiostat analyzer (ZIVE MP1, WonATech). A glassy carbon electrode (GCE; 5 mm diameter) served as the rotating disk electrode (RDE) in this setup. Prior to the experiments, each GCE was polished with alumina solution on a polishing cloth. For the electrocatalyst preparation, 5 mg of the catalysts (either Ex-PtCoWO NFs or a 'Pt/C + IrO₂' mixture) was blended with 50 μ L of Nafion™ 117 solution (5 wt%, Sigma Aldrich) as a binder and 1 mL of an organic solvent mixture (IPA: DI = 1:1 v/v). This mixture was subsequently sonicated for 1 h to achieve a homogeneous catalyst ink. Subsequently, 14 μ L of this ink was carefully dropped onto the GCE (loading density: 0.2 mg cm⁻²), ensuring complete coverage, and dried at 60 °C for 20 min. In the electrochemical setup, the catalyst-loaded GCE was utilized as the working electrode. A Hg/HgO electrode (saturated in 1 M NaOH) and a Pt coil were employed as the reference and counter electrodes, respectively.

Linear sweep voltammograms (LSVs) were recorded at a sweep rate of 5 mV s⁻¹. Chronoamperometry was performed at a constant potential. Electrochemical impedance spectroscopy (EIS) measurements were conducted at 1.6 V, over a frequency range from 100 kHz to 0.1 kHz under an alternating current (AC) voltage. The number of electrons (n) transferred during the ORR was calculated using the Koutecky–Levich (K-L) equations, denoted as Eqs. (2) and (3).

$$\frac{1}{J} = \frac{1}{J_L} + \frac{1}{J_k} = \frac{1}{bw^{1/2}} + \frac{1}{J_k} \quad (2)$$

$$b = 0.62nF C_0 (D_0)^{2/3} \nu^{-1/6} \quad (3)$$

where j , j_L , j_k , and ω are the measured disk current density, diffusion limiting current density, kinetic current density, and angular rotation rate (rad s⁻¹), respectively. F is the faradaic constant (96,485 C mol⁻¹), C_0 is the concentration of bulk oxygen in the electrolyte (1.26×10^{-6} mol cm⁻³ for 0.1 M KOH); D_0 is the diffusion coefficient of oxygen in the electrolyte (1.93×10^{-5} cm² s⁻¹ for 0.1 M KOH), and ν is the kinematic viscosity of the electrolyte (1.09×10^{-2} cm² s⁻¹ for 0.1 M KOH). Using this equation, we attempted to eliminate the mass transport effects from the measured currents to extract kinetic information during ORR. All measured potentials were calibrated to a reversible hydrogen electrode (RHE) potential using the Nernst Eq. (4):

$$E_{RHE} = E_{Hg/HgO} + E_{Hg^0/HgO}^0 + 0.059pH \quad (4)$$

2.7. Fabrication and performance evaluation of a container-type ZAB

The electrochemical performance of full cell tests was assessed using container-type ZAB cells. In these cells, a Zn foil (Alfa Aesar, 250 μ m-thick, 99.9%) served as the anode, while air electrodes were fashioned from Ex-PtCoWO NF-based catalysts sprayed onto a carbon cloth (loading density: 0.8 g cm⁻²). For control purposes in ZAB tests, air electrodes were similarly constructed using a mixture of commercial 20% Pt/C and IrO₂ (1:1 w/w) sprayed onto a carbon cloth (loading density: 0.8 g cm⁻²). The container-type cells were filled with 6 M KOH electrolyte. A non-woven carbon paper gas diffusion layer (GDL; SGL, 39BB) was utilized on the air cathode side to facilitate gas diffusion and selectively absorb O₂ from the ambient air. Additionally, a polytetrafluoroethylene (PTFE) membrane (SciLab) was incorporated as an additional layer to retard electrolyte evaporation. To evaluate the performance of the ZABs, initial charge and discharge behaviors, power

density, and cyclic performance were measured using a multichannel battery-testing system (WBCS3000L, Won-Atech) under ambient conditions (at 25 °C and 45% of relative humidity). The specifics of the measurement conditions are elaborated in the corresponding Results and Discussion section.

3. Results and discussion

3.1. Synthesis and morphological evolution of Ex-PtCoWO NFs

The comprehensive fabrication process of Ex-PtCoWO NFs is illustrated in Fig. 1. The synthesis began with the preparation of a homogeneous PVP solution, containing W, Co, and Pt precursors dissolved in DMF. This solution was loaded into a syringe for the electrospinning process, which was conducted under an applied voltage of 15 kV. The resultant as-spun composite NFs exhibited a smooth surface with an average diameter of 178 nm, as shown in Fig. S2. The as-spun NFs initially displayed no discernible crystalline peaks, with a broad shoulder in the 20–30° range, attributed to the turbostratic carbon structure present in the chain of PVP [43], as indicated by the XRD pattern in Fig. S3.

TGA was employed to investigate the thermal behavior of the precursors and PVP during calcination in air (Fig. S4). An initial weight reduction of about 15% was observed around 282 °C, mainly due to the evaporation of the organic solvent. This was followed by a notable weight loss between 282 and 396 °C, corresponding to the pyrolysis of the polymeric component and the decomposition of chloride and acetate precursors [44,45]. The weight continued to decrease up to 524 °C, due to the removal of organic residues, leaving approximately 35% of the initial weight from the as-spun fibers.

To optimize the ex-solution behavior in catalyst-support hybrids, we closely examined the microstructures of samples subjected to oxidation heat treatment at both 400 °C and 500 °C. As shown in Fig. S3, distinctive crystalline peaks were observed in the XRD patterns of the sample heat-treated at 400 °C, indicating a phase transition to the crystalline phases

WO₃ and CoWO₄ within PtCoWO NFs. Despite these phase transformations, the PtCoWO NFs retained their fibrous morphology, exhibiting an average diameter of 157 nm (Fig. S5). However, in the NF sample treated at 500 °C, significant grain growth and aggregation of Pt NPs were observed, with NP sizes reaching nearly 5.28 nm (Fig. S6). Notably, these pre-synthesized NPs were not expected to participate in the ex-solution process. Consequently, the primary heat treatment temperature was set to 400 °C in air, with the expectation that organic residues would be eliminated during subsequent high-temperature heat treatments.

The 2nd heat treatment of PtCoWO NFs involved thermal reduction at various temperatures (ranging from 500–800 °C, in 100 °C increments) in a 4% H₂/Ar atmosphere using a tube furnace. As the temperature increased, the color of the NFs transitioned from yellowish to darker shades, indicating a reduction in the bandgap of WO₃ and an expansion of the light absorption wavelength range (Fig. S7) [46]. Notably, the ex-solution behavior of multi-metallic components (Pt and Co) varied with the reduction temperature, as depicted in the inset of Fig. 1. In multi-component systems, variation in ex-solution behavior can be attributed to the reducibility of metal elements and their binding energy with lattice oxygen [25]. For instance, Pt ex-solution predominated at lower temperatures, while Co ex-solution became more significant at higher temperatures. Thus, we found that the presence of other metal components influences the ex-solution process. Excessive growth of ex-solved NPs was observed at the higher temperatures. This multi-component ex-solution phenomenon was thoroughly analyzed using a combination of microscopic and crystallographic techniques, supported by computational simulations.

The microstructural changes of Ex-PtCoWO NFs, as influenced by varying temperatures during the 2nd heat treatment, were explored using SEM images. Fig. 2a–d clearly illustrate that all samples maintained their overall nonwoven NF structures. Notably, as the heat treatment temperature increased, the mean diameter of NFs reduced from 147 to 125 nm, accompanied by an increase in surface roughness. Additionally, small pores became evident post 700 °C heat treatment

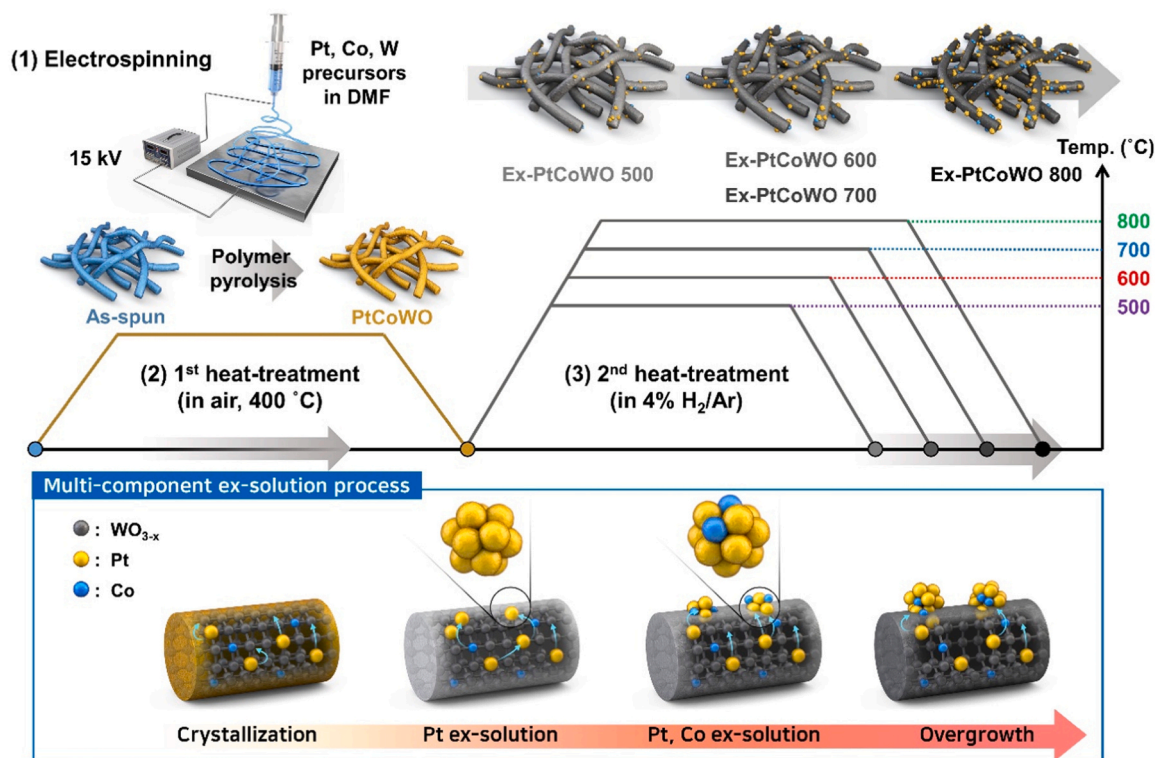


Fig. 1. Schematic of the fabrication procedure of Ex-PtCoWO NFs, including electrospinning, and the thermally-induced ex-solution process.

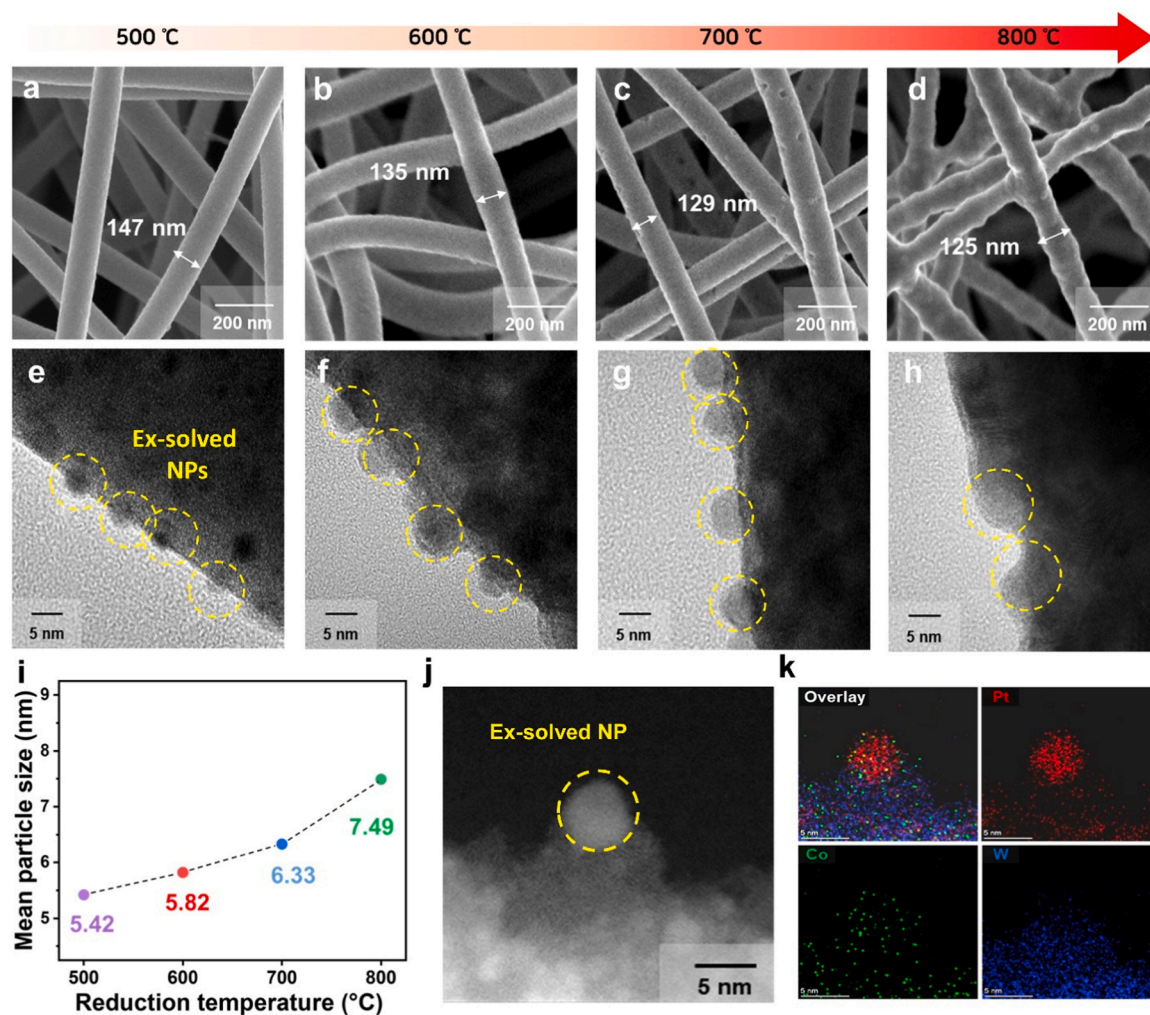


Fig. 2. Microstructure of Ex-PtCoWO NFs. (a–d) SEM images and (e–h) high-resolution TEM images of Ex-PtCoWO NFs obtained from the 2nd heat treatments at 500, 600, 700, and 800 °C, respectively. (i) Mean particle size analyses of ex-solved NPs for Ex-PtCoWO NFs. (j) High-angle annular dark-field scanning TEM (HAADF-STEM) image of Ex-PtCoWO 700 NF. (k) Energy dispersive X-ray spectrometry (EDS) mapping images with corresponding element maps of overlay, Pt (red), Co (green), and W (blue).

(Fig. 2c). These surface changes occur due to the volatilization of organic residues and the decomposition of the precursor materials. Further temperature elevation resulted in significant grain growth in the NFs (Fig. 2d), eventually leading to the disintegration of the one-dimensional (1D) fibrous structure in Ex-PtCoWO NFs treated at 900 °C, as shown in Fig. S8.

To delve deeper into the observed surface morphological changes, the specific surface areas of the NF samples, both before and after the reduction heat treatment, were analyzed via the BET method. The BET surface area of the Ex-PtCoWO 700 NF, depicted in Fig. S9, was found to be $13.91 \text{ m}^2 \text{ g}^{-1}$, approximately twice as high as that of the PtCoWO NF ($6.04 \text{ m}^2 \text{ g}^{-1}$). Furthermore, the pore volume of the Ex-PtCoWO 700 NF increased to $0.116 \text{ m}^3 \text{ g}^{-1}$ following the 2nd heat treatment, indicating an enhancement in both specific surface area and porosity, corroborating the SEM findings. O_2 -TPD analysis, shown in Fig. S10, was performed to assess the relationship between the surface characteristics of the catalyst O_2 . For each experiment, the sample was pretreated in a 5 % O_2 atmosphere for 1 h at 200 °C, then cooled in O_2 flow. Next, the sample was then purged with He gas and heated at a rate of $5 \text{ }^\circ\text{C per min}^{-1}$ up to 450 °C. In the case of ORR, high adsorption capacity of O_2 on the surface, is advantageous, whereas for OER, the easy detachment of O_2 after the reaction is favorable for continuous reactions. Peaks below 400 °C were linked to the desorption of physically adsorbed oxygen [47].

While the PtCoWO NF exhibited a lower oxygen desorption peak at 259 °C, the Ex-PtCoWO 700 NF showed a broader peak at a substantially lower temperature ($\sim 110 \text{ }^\circ\text{C}$), validating that the ex-solved sample augments oxygen adsorption and desorption on its surface, thereby enhancing catalytic activity [48,49].

TEM images, depicted in Fig. 2e–h, confirmed the presence of ex-solved metal NPs on the metal oxide NFs surface at all reduction temperatures. These NPs are small in size, indicating high dispersion and a large surface area, essential for surface reactivity. The mean particle size of the ex-solved NPs increased with rising temperature: 5.42, 5.82, 6.33, and 7.49 nm for Ex-PtCoWO 500, 600, 700, and 800 NFs, respectively, as indicated in Fig. 2i and Fig. S11. Notably, NPs ex-solved at 800 °C exhibited rapid clustering and growth, leading to their migration into the bulk region due to the enlarged pores created through the ex-solution phenomenon. High-resolution TEM (HRTEM) images revealed the overall NF structure with sparsely ex-solved NPs and the growth of larger particles resulting from the partial reduction of the WO_3 phase to metallic W (Fig. S12). Hence, Ex-PtCoWO 700 NF was selected for further analysis due to its uniform dispersion of ex-solved NPs and minimal particle growth.

HRTEM, HAADF-STEM, and EDS mapping were employed to examine the microstructure and atomic composition of the ex-solved NPs. HRTEM analysis of Ex-PtCoWO 700 NF revealed a lattice fringe

spacing of 0.223 nm, corresponding to the (111) plane of Pt, confirming the high crystallinity of Pt as indicated by fast Fourier transform (FFT) pattern (Fig. S13). EDS mapping of the ex-solved NPs on Ex-PtCoWO 700 NF showed that the majority of the NPs were composed of Pt, with a minor presence of Co atoms also detected within the ex-solved NP region (Fig. 2j-k and Fig. S14). This suggests a successful incorporation of Co into the Pt NPs, potentially enhancing their catalytic properties.

3.2. Chemical and crystallographic analysis of Ex-PtCoWO NFs

The structural transformations of Ex-PtCoWO NFs during the 2nd heat treatment were meticulously monitored using in-situ XRD analysis.

Fig. 3a illustrates the XRD patterns of PtCoWO NFs under a diluted H₂ atmosphere at a heating rate of 5 °C min⁻¹, mirroring the conditions of the fabrication process. Initially, the metal oxide phases (WO₃ and CoWO₄, denoted by dashed blue lines) persist up to 500 °C, subsequently undergoing thermal reduction to the WO_{2.73} phase (indicated by dashed green lines) in the temperature range of 600–700 °C. Beyond 800 °C, a further reduction to the metallic tungsten phase (W, highlighted by dashed red lines) is observed, with the W phase becoming predominant at 800 °C.

XPS analysis was employed to investigate the valence states and compositional elements of Ex-PtCoWO NFs. The emergence of metallic peaks verifies the ex-solution of metal NPs [50]. Initially, PtCoWO NFs

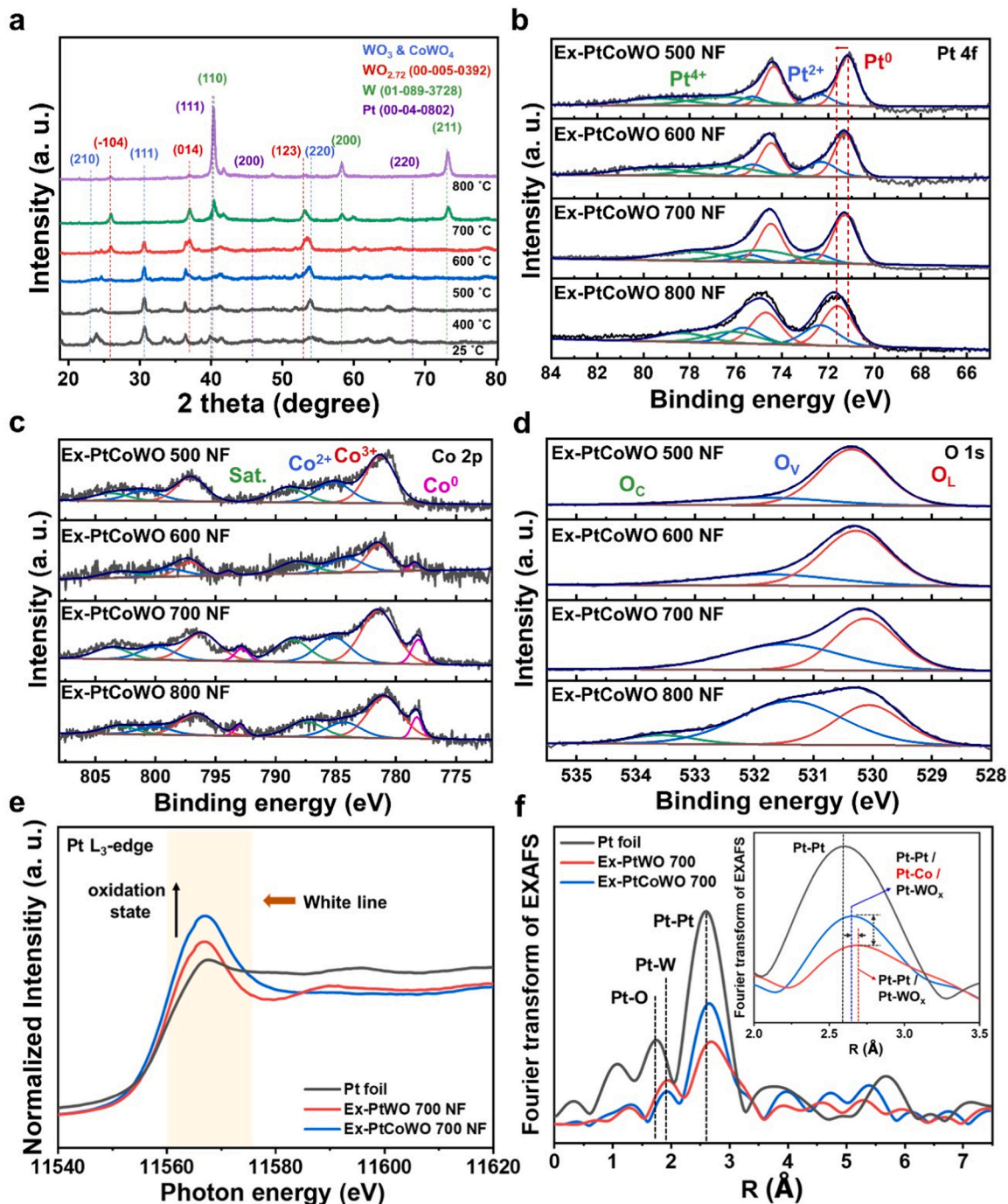


Fig. 3. (a) In-situ XRD patterns obtained from Ex-PtCoWO NFs in the temperature range of 25–800 °C. XPS spectra in (b) Pt 4f, (c) Co 2p, (d) O 1s region for Ex-PtCoWO NFs, (e) Pt L₃-edge XANES spectra, (f) simulated EXAFS-FT spectra. The details are placed within the orange box.

display spectra characteristic of high crystallinity metal oxides with elevated oxidation levels (Pt^{2+} and Pt^{4+}) (Fig. S15). Fig. 3b displays the Pt 4f spectra, where peaks at 71.1 and 74.3 eV correspond to the $4f_{7/2}$ and $4f_{5/2}$ peaks of Pt^0 , respectively. Furthermore, the distinct peak sets at 72.4 and 74.3 eV, and 76.8 and 79.3 eV are attributable to the $4f_{7/2}$ and $4f_{5/2}$ peaks of Pt^{2+} and Pt^{4+} in Ex-PtCoWO 500 NF, respectively [51]. Remarkably, even in Ex-PtCoWO 500 NF, which is subjected to a relatively low-temperature treatment, metallic peaks are predominantly observed. This is attributed to the high reducibility of Pt. The distinctive metallic peaks correlate closely with the ex-solved NPs as observed in Fig. 2e. Notably, the Pt^0 peaks shift from 71.1 eV to 71.6 eV with an increase in the temperature of the 2nd heat treatment, signifying a change in the electronic structure due to the interaction between metal NPs and the support material. This energy shift toward higher binding energies can also be explained by the chemical change attributed to the formation of a PtCo alloy, as evidenced in the EDS mapping in Fig. 2k [52,53]. The alteration in chemical states potentially supplies additional electrons, thereby enhancing ORR activity [54].

The Co 2p spectra were deconvoluted into Co^0 , Co^{2+} , Co^{3+} , and satellite peaks, each exhibiting doublet structures as depicted in Fig. 3c. The peaks of Co^{2+} (781.3 eV) and Co^{3+} (784.3 eV) indicate the presence of Co in the form of CoWO_4 within the bulk region. [55]. The appearance of the metallic Co^0 peak (778.1 eV) in Ex-PtCoWO 600 NF suggests the formation of metallic Co at temperatures exceeding 600 °C, attributable to its higher reduction potential compared to Pt. Notably, the proportion of metallic Co gradually increased from 5.4% to 8.7% as the reduction temperature increased. This indicates an ex-solution process in which metallic Co atoms are released from the support material. These metallic Co species likely contribute to the formation of a PtCo alloy, resulting in Co-doped Pt NPs on the surface of the support NFs.

The O 1s spectra were deconvoluted into O_L , O_V , and O_C peaks centered at 530.2, 531.5, and 533.5 eV, respectively (Fig. 3d). The O_L represents the surface lattice oxygen in the metal oxide support, O_V indicates oxygen vacancies, and the O_C refers to chemically adsorbed species such as water molecules or hydroxyl groups on the surface. The integrated peak area of O_V increased progressively during the reduction process, indicating a rise in the number of oxygen vacancies (Fig. S16c) [56,57]. Additionally, EPR spectroscopy was used to directly confirm the presence of oxygen vacancies in the NF. The EPR results corroborate the XPS analysis, showing a consistent trend of increasing oxygen vacancies (for further details, refer to Fig. S17). These generated oxygen defects are instrumental in altering the electronic structure of materials, thereby impacting electrical conductivity [58].

The chemical valence state and stoichiometry of W in the oxide NFs were confirmed in Fig. S18. Characteristic peaks at 37.81 eV and 35.69 eV correspond to W $4f_{5/2}$ and W $4f_{7/2}$ electrons, respectively, indicating the presence of W^{6+} species in the support NFs. As the reduction temperature rises, peaks corresponding to lower oxidation states of tungsten, specifically W^{5+} (33.7 eV), W^{4+} (32.3 eV), and metallic W^0 (31.4 eV), become more pronounced (Fig. S16d). This trend indicates a progressive reduction of tungsten oxides, further supporting the structural changes observed in the Ex-PtCoWO NFs. This finding suggests a partially nonstoichiometric crystalline surface structure, promoting the ex-solution and mobility of Pt and Co elements and enhancing charge transport [59]. However, the overall crystalline oxide structure is retained up to Ex-PtCoWO 700 NFs, as confirmed by XRD and the persistence of the W^{6+} peak.

XAS provided deeper insights into the local chemical structure of Ex-PtCoWO 700 NF. Fig. 3e displays the X-ray absorption near-edge structure (XANES) at the Pt L_3 edge for Ex-PtCoWO 700 NF and Ex-PtWO 700 NF, with a Pt foil as a reference. An elevated white line area in Ex-PtCoWO 700 NF indicates a higher oxidation state of Pt components in comparison to Pt foil. This white line intensity is reflective of the d orbital density of states, influenced by various oxidation states and electron configurations [60]. The increased integrated white line intensity observed in Ex-PtCoWO 700 NF indicates a

higher concentration of empty 5d orbital states (d holes), indicative of intensified interactions with Co atoms and the metal oxide support [61, 62]. Insights into the local structure of the catalysts are revealed in the EXAFS spectra. As shown in Fig. 3f, a prominent peak at 2.60 Å in the Pt L_3 -edge spectra signifies the nearest coordination shells of Pt atoms, and approximately 1.75 Å in the Pt L_3 -edge spectra indicates Pt-O bonds. The reduced intensity peak around 2.60 Å for Ex-PtCoWO 700 NF and Ex-PtWO 700 NF corresponds to the Pt-Pt bond, indicating the dispersion of the Pt cluster on the metal oxide support. Notably, a slight positive shift compared to Pt foil, and a negative shift compared to Ex-PtWO 700 NF, was observed. This implies an interaction between Co and the ex-solved Pt, as inferred from the simulated Pt-Pt length in Ex-PtCoWO 700 NF, leading to an alloying effect within Ex-PtCoWO 700 NF [63,64].

3.3. DFT calculation of multi-component ex-solution and their electrocatalytic activities

To elucidate the experimental observations regarding ex-solution, we conducted DFT calculations. These were performed in alignment with the experimental procedures, wherein the sequential ex-solution of Pt and Co on Ex-PtCoWO NFs occurred as the temperature increased. Initially, we constructed the CoWO_4 (100) surface, hereafter referred to as CoWO_4 , as the foundational structure. From this, two distinct structures were developed: PtCoWO_4 and Pt/CoWO_4 surfaces, with detailed descriptions provided in the computational section.

A key factor in these calculations is the formation of oxygen vacancies at elevated temperatures under H_2 gas purging, which can result in the reduction of metal atoms within the lattice structure. We postulate that the ex-solution process begins with the individual reduction of metal atoms within the lattice. For these metal atoms to aggregate into nanoclusters through surface diffusion or agglomeration, they must first break their bonds with oxygen atoms [25]. Based on this assumption, we suggest that the preferential ex-solution of metal components correlates with the strength of oxygen vacancy formation energy. Specifically, we propose that the presence of Pt clusters reduces the energy required for oxygen vacancy formation, thereby facilitating the ex-solution of Co. This occurs because the creation of oxygen vacancies is a crucial step for enabling the migration and agglomeration of Co atoms on the surface. Thus, Pt clusters play a significant role in facilitating Co ex-solution by modifying the local energy environment surrounding cobalt atoms. Therefore, we calculated the E_{vac} at various sites to determine which elements would be reduced first. For reference, we initially examined the E_{vac} near Co (2.44 eV) and W (2.91 eV) element sites, as illustrated in Fig. 4a. Although the positive E_{vac} values indicates that the formation of oxygen vacancies is energetically unfavorable, it remains plausible at high operating temperatures, which facilitate the reduction of metal elements.

For the PtCoWO_4 system, we analyzed three distinct sites: Co, W, and Pt. As depicted in Fig. 4b, the Pt site exhibited the lowest E_{vac} (2.56 eV), followed by the Co site (2.83 eV) and the W site (3.74 eV). These results suggest that oxygen vacancies are most likely to form near the Pt site, making Pt the preferred element for ex-solution due to its lower E_{vac} relative to Co and W. Following substantial Pt ex-solution, we hypothesized that ex-solved Pt atoms would tend to cluster. To evaluate the impact of Pt NPs on Co ex-solution, we considered two different Co sites: one proximal to the Pt NP (2.20 eV) and one distal (3.15 eV), as shown in Fig. 4c. Our calculations indicated that the formation of oxygen vacancies near Pt NPs resulted in the lowest E_{vac} across all Co sites, regardless of the system configuration. This suggests that the presence of Pt NPs significantly accelerates Co ex-solution by reducing the E_{vac} at nearby Co sites.

Another interesting aspect of this study was the observed changes in catalytic activity resulting from sequential ex-solution. Detailed experimental results will be discussed in subsequent section. Here, we focus on understanding and comparing the catalytic activity for ORR and OER across three different systems influenced by the ex-solution process:

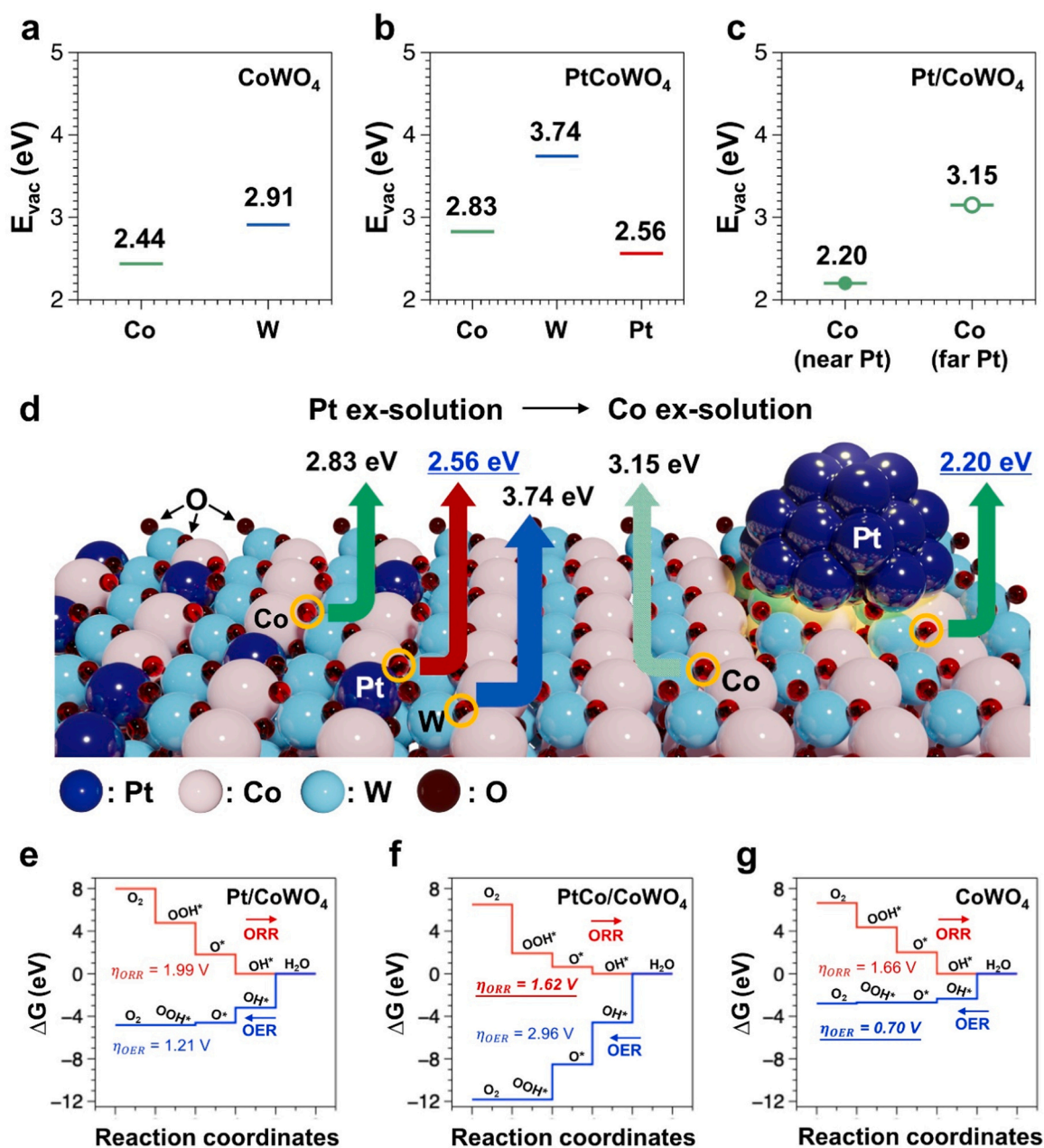


Fig. 4. DFT calculations results. Oxygen vacancy formation energy at different sites in (a) CoWO₄, (b) PtCoWO₄, and (c) Pt/CoWO₄. (d) Schematic of the sequential ex-solution mechanisms based on oxygen vacancy formation energy. Reaction energy diagram for ORR and OER on the (e) Pt/CoWO₄, (f) PtCo/CoWO₄, and (g) CoWO₄ systems, respectively.

CoWO₄, Pt/CoWO₄, and PtCo/CoWO₄. In DFT calculations, determining the overpotential based on the binding energy of potential adsorbates is a fundamental method to estimate the performance of electrochemical reactions [65,66]. A lower overpotential directly correlates with higher catalytic performance, indicating a smaller driving force needed to initiate the chemical reaction. We investigated all possible adsorbates and binding sites to identify the most plausible reaction pathway in each system. The reaction energy diagram for ORR (in red) and OER (in blue) are shown in the Fig. 4e-g.

In low-coordinated systems such as NPs, overly strong binding energy typically hinders the reaction, particularly in ORR, where strong OH binding energy presents a major obstacle. Alloying different elements into the Pt catalyst is a common strategy to weaken the OH binding energy. As shown in Fig. 4e-g, the reaction flattens in the final step (OH* → H₂O(l)) due to the strong OH binding energy. In other

words, the last step in ORR serves as the rate-determining step (RDS) in our systems. Consequently, the system with the weakest OH binding energy among CoWO₄ (-0.09 eV), Pt/CoWO₄ (-0.429 eV), and PtCo/CoWO₄ (-0.06 eV) exhibits the highest ORR activity. Based on the OH binding energy and reaction energy diagram, we assert that PtCo/CoWO₄ demonstrates the highest ORR activity.

For OER, the descriptor for activity estimation can differ as it is the reverse reaction of ORR. In this scenario, the first step (generation of OOH) serves as the RDS in NP-supported systems, except for CoWO₄. Similar to the ORR, strong OOH binding became a bottleneck in OER. Interestingly, CoWO₄ (3.121 eV) exhibits the weakest OOH binding energy compared to Pt/CoWO₄ (2.525 eV) and PtCo/CoWO₄ (0.774 eV) systems. The weak OOH binding energy in CoWO₄ alters the RDS. According to the overpotential calculations for both ORR and OER, we found that PtCo NPs formed through sequential ex-solution exhibit the

highest ORR activity, while the CoWO₄ support demonstrates the highest OER activity, based on binding energy calculations.

In summary, the E_{vac} calculations using DFT were employed to elucidate the mechanisms of sequential ex-solution. The oxygen near Pt atoms was predominantly vacated when Pt and Co were incorporated into the NFs. The formation of Pt NPs through the Pt ex-solution mechanism notably expedited the Co ex-solution process, as represented in Fig. 4d. These theoretical insights robustly corroborate the multi-component ex-solution phenomenon observed in the PtCoWO matrix, culminating in the formation of Co-doped Pt NPs, comparable to the series of experimental results.

3.4. Electrochemical half-cell performances

To evaluate the electrochemical performance of our synthesized samples, half-cell measurements were conducted using a three-electrode system, as depicted in Fig. 5. The working electrodes (catalysts loaded RDEs) were immersed in a 0.1 M KOH solution, which was purged with O₂ and Ar gas for the ORR and OER, respectively. Fig. 5a displays the LSV curves in the ORR region for Ex-PtCoWO NFs subjected to various 2nd heat treatment temperatures, alongside commercial Pt/C catalysts.

The half-wave potentials for Ex-PtCoWO 500 NF, Ex-PtCoWO 600 NF, Ex-PtCoWO 700 NF, Ex-PtCoWO 800 NF, and Pt/C are 0.69, 0.78, 0.89, 0.82, and 0.85 V versus RHE, respectively. This increase in half-wave potentials correlates with the progressive ex-solution of Pt and Co, which intensifies with rising heat-treatment temperatures. Notably, Ex-PtCoWO 700 NF demonstrated superior ORR performance compared to the other samples, even exceeding that of the commercial Pt/C catalyst. However, a decline in performance for Ex-PtCoWO 800 NF was observed, indicating that the coarsening of ex-solved NPs reduces the catalytically active surface area.

In the Tafel plot (Fig. 5b), the exceptional reaction kinetics of Ex-PtCoWO 700 NF are evident, with a Tafel slope of 103.0 mV dec⁻¹, lower than the 105.3 mV dec⁻¹ of Pt/C. As shown in Fig. 5c, the current density increased with rotational speeds ranging from 400 to 2025 rpm, indicating ORR activity in Ex-PtCoWO 700 NF. The electron-transfer number (*n*), derived using the Koutecký–Levich (K-L) equation (inset of Fig. 5c), for Ex-PtCoWO 700 NF was calculated to be 4.0. This result suggests that the catalyst favors a four-electron pathway in ORR, as further evidenced in Fig. S19 [67].

Fig. 5d presents the LSV curves of Ex-PtCoWO NFs and the commercial IrO₂ catalyst in the OER potential region. The trend in OER

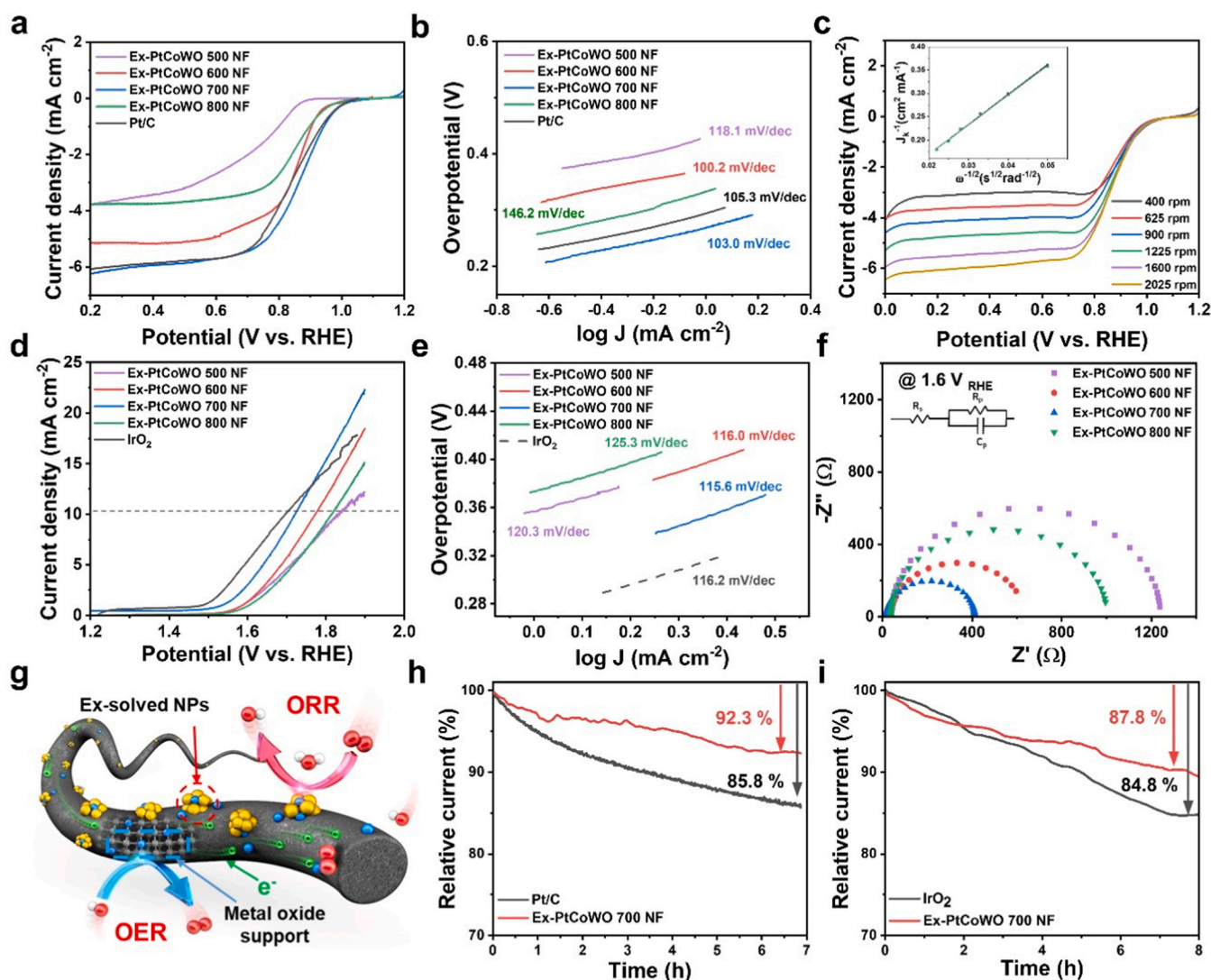


Fig. 5. Electrochemical half-cell performance and stability results in 0.1 M KOH. (a) ORR polarization curves for Ex-PtCoWO NFs and commercial Pt/C. (b) Tafel plot in the ORR regions derived from (a). (c) ORR polarization curves of Ex-PtCoWO 700 NF at different rotation electrode speeds (inset: K-L plot). (d) OER polarization curves for Ex-PtCoWO NFs and IrO₂. (e) Tafel plot at the OER regions derived from (d). (f) Nyquist plots of Ex-PtCoWO NFs. (g) The proposed reaction mechanism of Ex-PtCoWO NFs toward OER and ORR, chronoamperometry of Ex-PtCoWO NFs and commercial catalysts at (h) 0.8 V (ORR region) and (i) 1.6 V (OER region).

activity mirrors that of ORR, with Ex-PtCoWO 700 NF achieving the lowest voltage (1.69 V) required to reach an anodic current density of 10 mA cm^{-2} among the Ex-PtCoWO NFs, only slightly higher than the 1.68 V for IrO_2 . The Tafel slope of Ex-PtCoWO 700 NF is measured at $115.6 \text{ mV dec}^{-1}$, demonstrating comparability with other NFs and even the IrO_2 catalyst ($116.2 \text{ mV dec}^{-1}$), as illustrated in Fig. 5e. EIS Nyquist plots, depicted in Fig. 5f, were measured to assess the charge transfer resistance. Ex-PtCoWO 700 NF exhibits the smallest semicircle diameters compared to the other samples, suggesting higher OER kinetics attributable to improved charge transport in the catalysts. The overall overpotentials of Ex-PtCoWO NFs were compared, and Ex-PtCoWO 700 NF displayed the smallest overpotentials required to initiate ORR (0.34 V) and OER (0.46 V), as shown in Fig. S20. Furthermore, the exceptional bifunctional electrochemical performance of Ex-PtCoWO 700 NF is comparable to, and in some cases, even surpasses that of recently published Pt-based electrocatalysts (see Table S2).

To identify the active sites for each reaction, we synthesized Ex-PtWO 700 NF and Ex-CoWO 700 NF with component variations and compared their electrochemical performance. As indicated in Fig. S21, ORR activity was observed in the sample containing Pt atoms, whereas OER activity was evident in the CoWO_4 structure. Based on these additional half-cell measurements, a proposed reaction mechanism for Ex-PtCoWO NFs as bifunctional catalysts toward ORR and OER is

outlined in Fig. 5g. The ex-solved metal NPs play a crucial role in facilitating ORR. The superior ORR activity of Ex-PtCoWO 700 NF originates not only from the PtCo alloy, represented as Co-doped Pt NPs, but also from the robust interactions between the metal NPs and oxide supports, which enhance the oxygen redox reaction. Additionally, the 1D CoWO_4 NF matrix, characterized by a nonstoichiometric Co-incorporated WO_3 structure, serves as an active site for OER. This is evidenced by the fact that only the sample with the CoWO_4 NF matrix exhibited OER activity, as shown in Fig. S21. It also promotes charge transport and the migration of Pt and Co elements during ex-solution. The electrochemical measurement outcomes were found to correspond with the predictions derived from computational simulations, as evidenced by Fig. 4e-g.

Long-term stability is a crucial factor in assessing the practical applicability of bifunctional catalysts [68]. Stability tests for Ex-PtCoWO 700 NF and commercial catalysts were conducted in 0.1 M KOH using chronoamperometry measurements under potentials of 0.8 V and 1.6 V, with a rotational speed of 1600 rpm (Fig. S22). As shown in Fig. 5h, Ex-PtCoWO 700 NF retained 92.3% of its initial current density after a 7 h measurement period, whereas Pt/C preserved only 85.8% of its initial current. Similarly, Ex-PtCoWO 700 NF maintained over 87.8% of its initial OER performance, in contrast to commercial IrO_2 , which experienced an approximately 15.2% reduction in initial current density

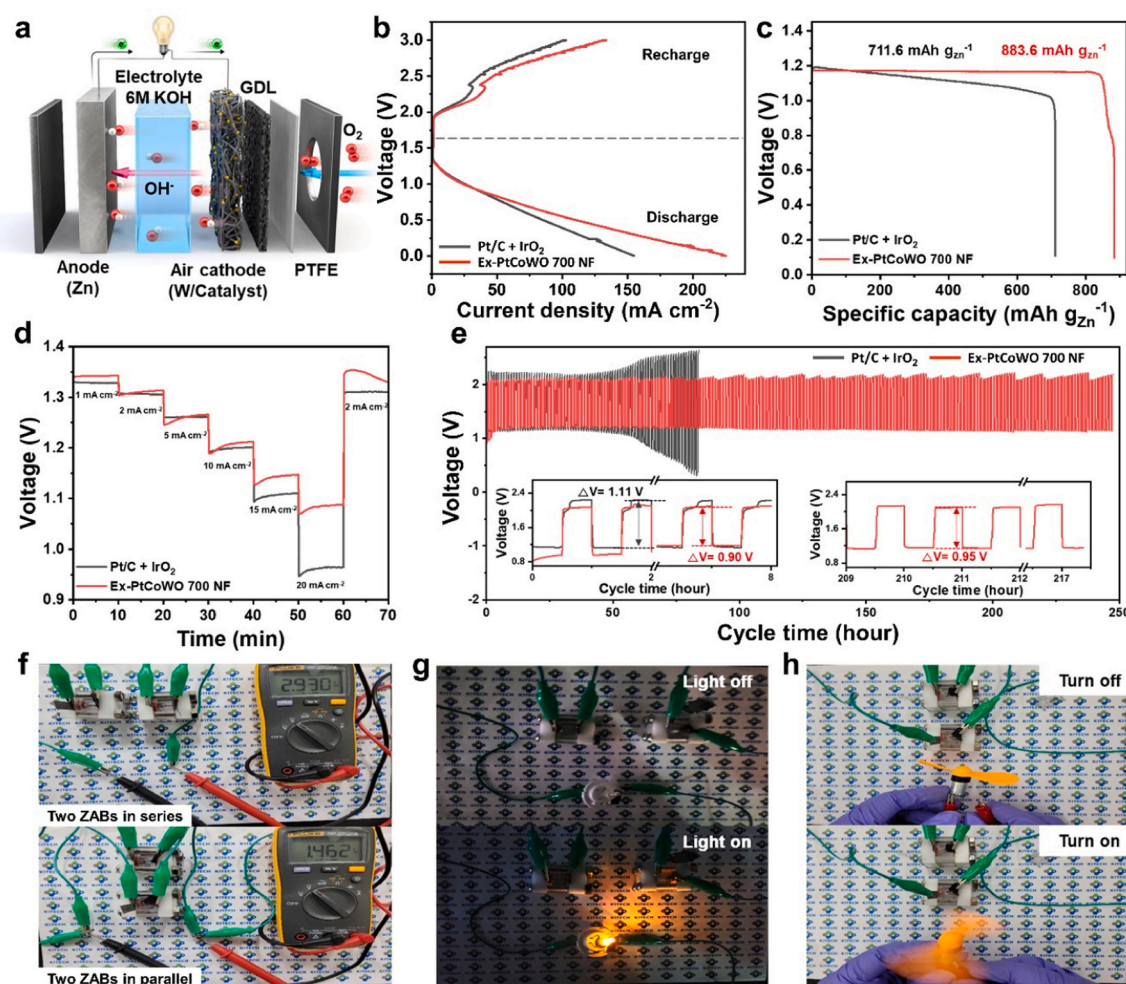


Fig. 6. Full-cell performances of container-type ZABs based on Ex-PtCoWO 700 NF and 'Pt/C + IrO_2 '. (a) Illustration of the air cathode with catalysts within the container-type ZABs. (b) Charge-discharge polarization curves. (c) Specific discharge capacity at a current density of 10 mA cm^{-2} . (d) Discharge voltage curves at different current densities, and (e) long cycling performance of ZABs at 2 mA cm^{-2} (insets: extended regions at the beginning and after 200 cycles). The digital photograph image of (f) OCV in two ZABs in series and parallel, (g) LED light (2.2 V) powered by two ZABs in series, and (h) operation of an electric fan operated by two ZABs in parallel.

after continuous OER operation for 8 h (Fig. 5i). To confirm the stability of the Ex-PtCoWO 700 NF catalyst after use, SEM and TEM images were taken (Fig. S23). The SEM images indicated no significant structural changes in the nanofibers during the chronoamperometry test for the ORR and OER regions, while TEM images showed that the particle size of the ex-solved metal nanoparticles remained 6.60 nm, as tested at 0.8 V, and 6.73 nm, as tested at 1.6 V. Additionally, the catalytic activity for ORR and OER was remeasured after the stability test (Fig. S24). Following the stability test conducted at 0.8 V, a decrease of 35 mV in the half-wave potential was observed, while after the stability test conducted at 1.6 V, the anodic current density of 10 mA cm^{-2} shifted positively by 23 mV. These results indicate that the ORR and OER performance of Ex-PtCoWO 700 NF experienced less degradation compared to commercial Pt/C or IrO₂, highlighting its excellent durability.

3.5. Full-cell performances in ZABs

To validate the practical applicability of the developed catalysts, we evaluated the full-cell performance using container-type ZABs. The schematic configuration of the container-type ZAB is depicted in Fig. 6a. In the air cathode construction, the catalysts either Ex-PtCoWO 700 NF or a mixture of 'Pt/C + IrO₂' were applied to carbon cloth using the air-spray method. A GDL and a PTFE membrane were employed as supporting layers to facilitate air breathing and prevent electrolyte leakage through the open side of container, respectively. Zn foil served as the anode, and the container was filled with a 6 M KOH solution as the electrolyte. A photograph of the actual cell used in this work is shown in Fig. S25.

As depicted in Fig. S26, the cell utilizing Ex-PtCoWO 700 NF maintained its open-circuit voltage (OCV) at approximately 1.45 V for 8 h with almost negligible self-discharge. Fig. 6b presents the charge-discharge polarization curves of cells using Ex-PtCoWO 700 NF compared to the 'Pt/C + IrO₂' mixture. The lower charge-discharge polarization and increased capacities observed in the Ex-PtCoWO 700 NF cell can be attributed to its superior bifunctional catalytic activities, as indicated by the half-cell measurements. The discharge power density of the cells using Ex-PtCoWO 700 NF reveals a peak power density of 55 mW cm^{-2} at 105 mA cm^{-2} (Fig. S27), which exceeds that of the cell using 'Pt/C + IrO₂' (43 mW cm^{-2} at 71 mA cm^{-2}).

Fig. 6c showed the galvanostatic discharge curves of cells using Ex-PtCoWO 700 NF and 'Pt/C + IrO₂'. The specific capacity was calculated based on the weight of zinc anode. The ZAB incorporating Ex-PtCoWO 700 NF exhibits a higher specific capacity of 883.6 mAh g^{-1} , compared to 711.6 mAh g^{-1} for the 'Pt/C + IrO₂' cell, indicating its superior energy density due to enhanced ORR stability. Furthermore, we compared the discharge rate performance at various current densities. The discharge potential plateaus of Ex-PtCoWO 700 NF were higher than those of 'Pt/C + IrO₂' at increased current densities, specifically up to 20 mA cm^{-2} (Fig. 6d). Even at a current density of 20 mA cm^{-2} , the Ex-PtCoWO 700 NF cell maintained outstanding performance with a discharge voltage of 1.09 V. Galvanostatic cycling tests were conducted at a current density of 2 mA cm^{-2} for 30 min per cycle, as shown in Fig. 6e. The Ex-PtCoWO 700 NF cell demonstrated stable cycle performance in the ZAB for 244 h, with a smaller voltage gap compared to the cell using commercial catalysts. Notably, as highlighted in the inset images, there were no significant voltage gap changes over 200 h (remaining between 0.90 and 0.95 V), whereas severe voltage polarization was observed in cells using 'Pt/C + IrO₂' within less than 100 h.

Fig. 6f illustrates the stable OCV of ZABs with Ex-PtCoWO 700 NF catalysts connected in series, almost doubling the voltage compared to ZABs in parallel. The series-connected two ZABs were able to supply adequate operational voltage to power a 2.2 V LED light (Fig. 6g). Additionally, the two ZABs in parallel successfully operated a fan requiring a 15 W motor (Fig. 6h). These demonstrations highlight the versatility and practical applicability of Ex-PtCoWO 700 NF catalysts in powering a wide range of electronic devices.

4. Conclusion

In summary, The Ex-PtCoWO 700 NF, a catalyst-support hybrid, was successfully synthesized via electrospinning followed by a thermal ex-solution process. This material exhibited superior ORR/OER activity, along with notable stability in alkaline environments. DFT calculations shed light on the mechanisms underpinning sequential ex-solution, particularly highlighting the preferential ex-solution of Pt, followed by Co, and elucidating the catalytic role of Pt NPs in expediting the ex-solution of Co. Moreover, rechargeable ZABs constructed with Ex-PtCoWO 700 NF demonstrated remarkable durability, higher power density, lower voltage gap, and improved cyclic charge/discharge performance compared to commercial catalysts, showcasing their feasibility for various electronic devices. We believe that this study introduces a synergistic ex-solution mechanism in a multi-component system, which could inspire the design of hybrid catalyst support system. Moreover, considering the rarity of ex-solution generated from NF-type oxide supports for ZAB air cathode materials, this work is expected to expand the scope of metal catalyst-oxide support materials for air batteries.

CRedit authorship contribution statement

Sunyong Caroline Lee: Writing – review & editing, Validation, Supervision. **Ki Ro Yoon:** Writing – review & editing, Visualization, Validation, Supervision, Resources, Project administration, Conceptualization. **Kihyun Shin:** Software, Data curation, Conceptualization. **Jong Min Kim:** Validation, Resources, Investigation. **Changho Lee:** Writing – original draft, Visualization, Methodology, Investigation, Formal analysis, Data curation, Conceptualization. **Chang-Kyu Hwang:** Validation, Investigation, Data curation. **Jung-Won An:** Validation, Investigation. **Ji-Soo Jang:** Resources, Investigation. **Bonjae Koo:** Resources, Investigation.

Declaration of Competing Interest

The authors declare that they have no known competing financial interests or personal relationships that could have appeared to influence the work reported in this paper.

Data Availability

The authors do not have permission to share data.

Acknowledgements

This research was supported by National Research Foundation of Korea (NRF) grant funded by the Korean government (MSIT) (No. 2022R1F1A1068725 and 202300000002243) and GRDC (Global Research Development Center) Cooperative Hub Program through the National Research Foundation of Korea (NRF) funded by the Ministry of Science and ICT (MSIT) (RS-2023-00257595). We would like to thank Editage (www.editage.co.kr) for English language editing.

Appendix A. Supporting information

Supplementary data associated with this article can be found in the online version at [doi:10.1016/j.apcatb.2024.124371](https://doi.org/10.1016/j.apcatb.2024.124371).

References

- [1] J. Wang, Y. Li, X. Sun, Challenges and opportunities of nanostructured materials for aprotic rechargeable lithium-air batteries, *Nano Energy* 2 (2013) 443–467.
- [2] V. Caramia, B. Bozzini, Materials science aspects of zinc-air batteries: a review, *J. Renew. Sustain. Energy* 3 (2014) 1–12.
- [3] Y. Li, J. Fu, C. Zhong, T. Wu, Z. Chen, W. Hu, K. Amine, J. Lu, Recent advances in flexible zinc-based rechargeable batteries, *Adv. Energy Mater.* 9 (2019) 1802605.

- [4] J.S. Lee, S. Tai Kim, R. Cao, N.S. Choi, M. Liu, K.T. Lee, J. Cho, Metal-air batteries with high energy density: Li-air versus Zn-air, *Adv. Energy Mater.* 1 (2011) 34–50.
- [5] W.T. Hong, M. Risch, K.A. Stoerzinger, A. Grimaud, J. Suntivich, Y. Shao-Horn, Toward the rational design of non-precious transition metal oxides for oxygen electrocatalysis, *Energy Environ. Sci.* 8 (2015) 1404–1427.
- [6] J.C. Meier, C. Galeano, I. Katsounaros, J. Witte, H.J. Bongard, A.A. Topalov, C. Baldizzone, S. Mezzavilla, F. Schütz, K.J. Mayrhofer, Design criteria for stable Pt/C fuel cell catalysts, *Beilstein J. Nanotechnol.* 5 (2014) 44–67.
- [7] C. Ye, M. Zheng, Z. Li, Q. Fan, H. Ma, X. Fu, D. Wang, J. Wang, Y. Li, Electrical Pulse Induced One-step Formation of Atomically Dispersed Pt on Oxide Clusters for Ultra-Low-Temperature Zinc-Air Battery, *Angew. Chem. Int. Ed.* 61 (2022) e202213366.
- [8] Y. Li, Y. Deng, D. Liu, Q. Ji, X. Cai, Two dimensional oxides for oxygen evolution reactions and related device applications, *Mater. Chem. Front.* (2024).
- [9] H. Lv, S. Mu, Nano-ceramic support materials for low temperature fuel cell catalysts, *Nanoscale* 6 (2014) 5063–5074.
- [10] D. Neagu, T.-S. Oh, D.N. Miller, H. Ménard, S.M. Bukhari, S.R. Gamble, R.J. Gorte, J.M. Vohs, J.T. Irvine, Nano-socketed nickel particles with enhanced coking resistance grown in situ by redox exsolution, *Nat. Commun.* 6 (2015) 8120.
- [11] A. Saad, Y. Gao, A. Ramiere, T. Chu, G. Yasin, Y. Wu, S. Ibraheem, M. Wang, H. Guo, P. Tsiarakas, Understanding the Surface Reconstruction on Ternary WxCoBx for Water Oxidation and Zinc-Air Battery Applications, *Small* 18 (2022) 2201067.
- [12] Z. Song, J. Zhao, U. Ghani, W. Liu, B. Ye, X. Cai, Metal Organic Frameworks Derived Layered Double Hydroxide Nanosheets for Electrochemical Energy Storage and Conversion, *ChemElectroChem* (2024) e202300731.
- [13] K. Wang, J. Lu, Y. Lu, C.H. Lau, Y. Zheng, X. Fan, Unravelling the CC coupling in CO₂ photocatalytic reduction with H₂O on Au/TiO₂-x: Combination of plasmonic excitation and oxygen vacancy, *Appl. Catal. B* 292 (2021) 120147.
- [14] Z. Pan, Y. Xiao, Z. Fu, G. Zhan, S. Wu, C. Xiao, G. Hu, Z. Wei, Hollow and porous titanium nitride nanotubes as high-performance catalyst supports for oxygen reduction reaction, *J. Mater. Chem.* 2 (2014) 13966–13975.
- [15] S.-H. Cho, K.R. Yoon, K. Shin, J.-W. Jung, C. Kim, J.Y. Cheong, D.-Y. Youn, S. W. Song, G. Henkelman, I.-D. Kim, Synergistic coupling of metallic cobalt nitride nanofibers and IrO_x nanoparticle catalysts for stable oxygen evolution, *Chem. Mater.* 30 (2018) 5941–5950.
- [16] Z. Fang, L.-C. Wang, Y. Wang, E. Sikorski, S. Tan, K.D. Li-Oakey, L. Li, G. Yablonsky, D.A. Dixon, R. Fushimi, Pt-assisted carbon remediation of Mo₂C catalysts for CO disproportionation, *ACS Catal.* 10 (2020) 1894–1911.
- [17] O. Lori, S. Gonen, O. Kapon, L. Elbaz, Durable tungsten carbide support for Pt-based fuel cells cathodes, *ACS Appl. Mater. Interfaces* 13 (2021) 8315–8323.
- [18] L. Wang, Z. Xu, C.H. Kuo, J. Peng, F. Hu, L. Li, H.Y. Chen, J. Wang, S. Peng, Stabilizing low-valence single atoms by constructing metalloid tungsten carbide supports for efficient hydrogen oxidation and evolution, *Angew. Chem. Int. Ed.* 62 (2023) e202311937.
- [19] G.Y. Kim, K.R. Yoon, K. Shin, J.W. Jung, G. Henkelman, W.H. Ryu, Black tungsten oxide nanofiber as a robust support for metal catalysts: high catalyst loading for electrochemical oxygen reduction, *Small* 17 (2021) 2103755.
- [20] M. Hossain, K. Sarkar, A. Mondal, A. Bag, P.K. Kuir, M.S. Roopa, S. Kumar, P. Bysakh, Pal, NO₂ gas sensing performance of Ag–WO₃–x thin films prepared by reactive magnetron sputtering process, *Appl. Phys. A* 129 (2023) 866.
- [21] T. Paik, M. Cargnello, T.R. Gordon, S. Zhang, H. Yun, J.D. Lee, H.Y. Woo, S.J. Oh, C.R. Kagan, P. Fornasiero, Photocatalytic hydrogen evolution from substoichiometric colloidal WO₃-x nanowires, *ACS Energy Lett.* 3 (2018) 1904–1910.
- [22] P.A. Shinde, S.C. Jun, Review on recent progress in the development of tungsten oxide based electrodes for electrochemical energy storage, *ChemSusChem* 13 (2020) 11–38.
- [23] Q. Han, X. Zhao, Y. Luo, L. Wu, S. Sun, J. Li, Y. Wang, G. Liu, Z. Chen, Synergistic Binary Fe–Co Nanocluster Supported on Defective Tungsten Oxide as Efficient Oxygen Reduction Electrocatalyst in Zinc-Air Battery, *Adv. Sci.* 9 (2022) 2104237.
- [24] Y. Zhang, X. Ma, K. Zhu, J. Wang, Z. Cheng, G. Li, L. Yang, Z. Bai, Hybrid Co/CoO/Ce-Doped WO₃ Nanoparticles on a ZIF-L Framework as Bifunctional Oxygen Electrocatalysts for Rechargeable Zinc-Air Batteries, *ACS Appl. Nano Mater.* 6 (2023) 14353–14363.
- [25] J.H. Kim, J.K. Kim, J. Liu, A. Curcio, J.-S. Jang, I.-D. Kim, F. Ciucci, W. Jung, Nanoparticle ex-solution for supported catalysts: materials design, mechanism and future perspectives, *ACS nano* 15 (2020) 81–110.
- [26] D. Neagu, G. Tsekouras, D.N. Miller, H. Ménard, J.T. Irvine, In situ growth of nanoparticles through control of non-stoichiometry, *Nat. Chem.* 5 (2013) 916–923.
- [27] Y.-R. Jo, B. Koo, M.-J. Seo, J.K. Kim, S. Lee, K. Kim, J.W. Han, W. Jung, B.-J. Kim, Growth kinetics of individual Co particles ex-solved on SrTiO₃. 25O₃-δ polycrystalline perovskite thin films, *J. Am. Chem. Soc.* 141 (2019) 6690–6697.
- [28] P. Anand, M.-S. Wong, Y.-P. Fu, Perovskite oxide composites for bifunctional oxygen electrocatalytic activity and zinc-air battery application-A mini-review, *Energy Storage Mater.* (2023).
- [29] Y. Lu, Y. Jiang, X. Gao, X. Wang, W. Chen, Strongly coupled Pd nanotetrahedron/tungsten oxide nanosheet hybrids with enhanced catalytic activity and stability as oxygen reduction electrocatalysts, *J. Am. Chem. Soc.* 136 (2014) 11687–11697.
- [30] X. Hu, K. Xie, Active and stable Ni/Cr₂O₃-δ cathodes for high temperature CO₂ electrolysis, *J. Power Sources* 430 (2019) 20–24.
- [31] S.H. Kim, H. Jeong, B. Sharma, J.-h Myung, In situ exsolution catalyst: an innovative approach to develop highly selective and sensitive gas sensors, *ACS Appl. Mater. Interfaces* 14 (2022) 18275–18282.
- [32] J.S. Jang, J.K. Kim, K. Kim, W.G. Jung, C. Lim, S. Kim, D.H. Kim, B.J. Kim, J. W. Han, W. Jung, Dopant-Driven Positive Reinforcement in Ex-Solution Process: New Strategy to Develop Highly Capable and Durable Catalytic Materials, *Adv. Mater.* 32 (2020) 2003983.
- [33] G. Kresse, D. Joubert, From ultrasoft pseudopotentials to the projector augmented-wave method, *Phys. Rev. B* 59 (1999) 1758.
- [34] G. Kresse, J. Furthmüller, Efficiency of ab-initio total energy calculations for metals and semiconductors using a plane-wave basis set, *Comput. Mater. Sci.* 6 (1996) 15–50.
- [35] G. Kresse, J. Hafner, Ab initio molecular dynamics for liquid metals, *Phys. Rev. B* 47 (1993) 558.
- [36] Y. Zhang, W. Yang, Comment on “Generalized gradient approximation made simple”, *Phys. Rev. Lett.* 80 (1998) 890.
- [37] J.P. Perdew, K. Burke, M. Ernzerhof, Generalized gradient approximation made simple, *Phys. Rev. Lett.* 77 (1996) 3865.
- [38] B. Hammer, L.B. Hansen, J.K. Nørskov, Improved adsorption energetics within density-functional theory using revised Perdew-Burke-Ernzerhof functionals, *Phys. Rev. B* 59 (1999) 7413.
- [39] J.K. Nørskov, J. Rossmeisl, A. Logadottir, L. Lindqvist, J.R. Kitchin, T. Bligaard, H. Jonsson, Origin of the overpotential for oxygen reduction at a fuel-cell cathode, *J. Phys. Chem. B* 108 (2004) 17886–17892.
- [40] J. Rossmeisl, G.S. Karlberg, T. Jaramillo, J.K. Nørskov, Steady state oxygen reduction and cyclic voltammetry, *Farad. Disc.* 140 (2009) 337–346.
- [41] I.C. Man, H.Y. Su, F. Calle-Vallejo, H.A. Hansen, J.I. Martínez, N.G. Inoglu, J. Kitchin, T.F. Jaramillo, J.K. Nørskov, J. Rossmeisl, Universality in oxygen evolution electrocatalysis on oxide surfaces, *ChemCatChem* 3 (2011) 1159–1165.
- [42] A.A. Peterson, F. Abild-Pedersen, F. Studt, J. Rossmeisl, J.K. Nørskov, How copper catalyzes the electroreduction of carbon dioxide into hydrocarbon fuels, *Energy Environ. Sci.* 3 (2010) 1311–1315.
- [43] K.R. Yoon, K. Shin, J. Park, S.-H. Cho, C. Kim, J.-W. Jung, J.Y. Cheong, H.R. Byon, H.M. Lee, I.-D. Kim, Brush-like cobalt nitride anchored carbon nanofiber membrane: current collector-catalyst integrated cathode for long cycle Li–O₂ batteries, *ACS nano* 12 (2018) 128–139.
- [44] K.R. Yoon, J.W. Ko, D.-Y. Youn, C.B. Park, I.-D. Kim, Synthesis of Ni-based co-catalyst functionalized W: BiVO₄ nanofibers for solar water oxidation, *Green. Chem.* 18 (2016) 944–950.
- [45] D. Gutiérrez-Martín, A. Varela, J.M. González-Calbet, E. Mateo, M. Parras, Revisiting the decomposition process of tetrahydrate Co (II) acetate: a sample’s journey through temperature, *Appl. Sci.* 12 (2022) 6786.
- [46] X. Liu, G. Zhu, X. Wang, X. Yuan, T. Lin, F. Huang, Progress in black titania: a new material for advanced photocatalysis, *Energy Storage Mater.* 6 (2016) 1600452.
- [47] B. Kayaalp, S. Lee, K. Klauke, J. Seo, L. Nodari, A. Kornowski, W. Jung, S. Mascotto, Template-free mesoporous La_{0.3}Sr_{0.7}Ti_{1-x}FexO_{3±δ} for CH₄ and CO oxidation catalysis, *Appl. Catal. B* 245 (2019) 536–545.
- [48] B. Zhang, G. Cheng, B. Lan, X. Zheng, M. Sun, F. Ye, L. Yu, X. Cheng, Crystallization design of MnO₂ via acid towards better oxygen reduction activity, *CrystEngComm* 18 (2016) 6895–6902.
- [49] S. Kim, J.-W. Jung, D. Song, S.-H. Cho, J. Kim, J.K. Kim, D. Oh, H. Sun, E. Cho, I.-D. Kim, Exceptionally durable CoFe-exsolved Sr_{0.95}Nb_{0.1}Co_{0.7}Fe_{0.2}O_{3-δ} catalyst for rechargeable Zn-air batteries, *Appl. Catal. B* 315 (2022) 121553.
- [50] A. Nennig, J. Fleig, Electrochemical XPS investigation of metal exsolution on SOFC electrodes: Controlling the electrode oxygen partial pressure in ultra-high-vacuum, *Surf. Sci.* 680 (2019) 43–51.
- [51] R.-M. Sun, R.-Z. Wu, X.-S. Li, J.-J. Feng, L. Zhang, A.-J. Wang, Well entrapped platinum-iron nanoparticles on three-dimensional nitrogen-doped ordered mesoporous carbon as highly efficient and durable catalyst for oxygen reduction and zinc-air battery, *J. Colloid Interface Sci.* 621 (2022) 275–284.
- [52] B.S. Mun, M. Watanabe, M. Rossi, V. Stamenkovic, N.M. Markovic, P.N. Ross, A study of electronic structures of Pt₃M (M = Ti, V, Cr, Fe, Co, Ni) polycrystalline alloys with valence-band photoemission spectroscopy, *J. Chem. Phys.* 123 (2005).
- [53] S. Hida, M. Kobayashi, H. Niwa, Y. Harada, M. Oshima, Y. Nakamori, T. Aoki, Changes in electronic states of platinum-cobalt alloy catalyst for polymer electrolyte fuel cells by potential cycling, *J. Power Sources* 196 (2011) 8340–8345.
- [54] C. Jackson, G.T. Smith, D.W. Inwood, A.S. Leach, P.S. Whalley, M. Callisti, T. Polcar, A.E. Russell, P. Levecque, D. Kramer, Electronic metal-support interaction enhanced oxygen reduction activity and stability of boron carbide supported platinum, *Nat. Commun.* 8 (2017) 15802.
- [55] P. Bagwade, V. Magdum, D. Malavekar, Y. Chitare, J. Gunjekar, U. Patil, C. Lokhande, Synthesis, characterization and visible light driven dye degradation performance of one-pot synthesized amorphous CoWO₄ powder, *J. Mater. Sci.: Mater. Electron.* 33 (2022) 24646–24662.
- [56] K. Jing, W. Ma, Y. Ren, J. Xiong, B. Guo, Y. Song, S. Liang, L. Wu, Hierarchical Bi₂MoO₆ spheres in situ assembled by monolayer nanosheets toward photocatalytic selective oxidation of benzyl alcohol, *Appl. Catal. B* 243 (2019) 10–18.
- [57] X. Huang, X. Gao, Q. Xue, C. Wang, R. Zhang, Y. Gao, Z. Han, Impact of oxygen vacancies on TiO₂ charge carrier transfer for photoelectrochemical water splitting, *Dalton Trans.* 49 (2020) 2184–2189.
- [58] Y. Cheng, J. Kang, P. Yan, J. Shen, Z. Chen, X. Zhu, Q. Tan, L. Shen, S. Wang, S. Wang, Surface oxygen vacancies prompted the formation of hydrated hydroxyl groups on ZnOx in enhancing interfacial catalytic ozonation, *Appl. Catal. B* 341 (2024) 123325.
- [59] X. Zhang, W. Hao, C.-S. Tsang, M. Liu, G.S. Hwang, L.Y.S. Lee, Pseudocubic phase tungsten oxide as a photocatalyst for hydrogen evolution reaction, *ACS Appl. Energy Mater.* 2 (2019) 8792–8800.
- [60] J. Xing, H.B. Jiang, J.F. Chen, Y.H. Li, L. Wu, S. Yang, L.R. Zheng, H.F. Wang, P. Hu, H.J. Zhao, Active sites on hydrogen evolution photocatalyst, *J. Mater. Chem. A* 1 (2013) 15258–15264.

- [61] S. Sun, G. Zhang, N. Gauquelin, N. Chen, J. Zhou, S. Yang, W. Chen, X. Meng, D. Geng, M.N. Banis, Single-atom catalysis using Pt/graphene achieved through atomic layer deposition, *Sci. Rep.* 3 (1) (2013) 9.
- [62] H. Wei, X. Liu, A. Wang, L. Zhang, B. Qiao, X. Yang, Y. Huang, S. Miao, J. Liu, T. Zhang, FeOx-supported platinum single-atom and pseudo-single-atom catalysts for chemoselective hydrogenation of functionalized nitroarenes, *Nat. Commun.* 5 (2014) 5634.
- [63] S. Yang, J. Kim, Y.J. Tak, A. Soon, H. Lee, Single-atom catalyst of platinum supported on titanium nitride for selective electrochemical reactions, *Angew. Chem. Int. Ed.* 55 (2016) 2058–2062.
- [64] L.-C. Lin, C.-H. Kuo, Y.-H. Hsu, L.-C. Hsu, H.-Y. Chen, J.-L. Chen, Y.-T. Pan, High-performance intermetallic PtCo oxygen reduction catalyst promoted by molybdenum, *Appl. Catal. B* 317 (2022) 121767.
- [65] K.R. Yoon, C.-K. Hwang, S.-h Kim, J.-W. Jung, J.E. Chae, J. Kim, K.A. Lee, A. Lim, S.-H. Cho, J.P. Singh, Hierarchically assembled cobalt oxynitride nanorods and N-doped carbon nanofibers for efficient bifunctional oxygen electrocatalysis with exceptional regenerative efficiency, *ACS nano* 15 (2021) 11218–11230.
- [66] Y. Gao, Y. Yang, L. Hao, S. Hong, X. Tan, T.-S. Wu, Y.-L. Soo, A.W. Robertson, Q. Yang, Z. Sun, Single Nb atom modified anatase TiO₂ (110) for efficient electrocatalytic nitrogen reduction reaction, *Chem. Catal.* 2 (2022) 2275–2288.
- [67] X. Cheng, Y. Wang, Y. Lu, L. Zheng, S. Sun, H. Li, G. Chen, J. Zhang, Single-atom alloy with Pt-Co dual sites as an efficient electrocatalyst for oxygen reduction reaction, *Appl. Catal. B* 306 (2022) 121112.
- [68] D. Kundu, B.D. Adams, V. Duffort, S.H. Vajargah, L.F. Nazar, A high-capacity and long-life aqueous rechargeable zinc battery using a metal oxide intercalation cathode, *Nat. Energy* 1 (2016) 1–8.